USING NARROWBAND PHOTOMETRY TO CLASSIFY STARS AND BROWN DWARFS

A. K. Mainzer,[1,2] Ian S. McLean,[1] J. L. Sievers,[3] and E. T. Young[4]

ABSTRACT

We present a new system of narrowband filters in the near-infrared that can be used to classify stars and brown dwarfs. This set of four filters, spanning the H band, can be used to identify molecular features unique to brown dwarfs, such as H_2O and CH_4. The four filters are centered at 1.495 μm (H_2O), 1.595 μm (continuum), 1.66 μm (CH_4), and 1.75 μm (H_2O). Using two H_2O filters allows us to solve for the reddening of individual objects. This can be accomplished by constructing a color-color-color cube and rotating it until the reddening vector disappears. We created a model of predicted color-color-color values for different spectral types by integrating filter bandpass data with the spectra of known stars and brown dwarfs. We validated this model by making photometric measurements of seven known L and T dwarfs, ranging from L1 to T7.5. The photometric measurements agree with the model to within ±0.1 mag, allowing us to create spectral indexes for different spectral types. We can classify A through early M stars to within ±2 spectral types, late-type M and L dwarfs to within ±0.3 spectral types, and T dwarfs to within ±0.1 spectral types (1 σ). Thus, we can distinguish between a T1 and a T3 dwarf. The four physical bands can be converted into two reddening-free indexes μ_1 and μ_2 and an extinction A_V for the individual objects. This technique, which is equivalent to extremely low resolution spectroscopy, can be used to survey large areas to provide rough spectral classifications for all the stars in the area, ranging down to the coolest brown dwarfs. It should prove particularly useful in young clusters where reddening can be high.

Subject headings: infrared: stars — stars: formation — stars: low-mass, brown dwarfs — stars: pre–main-sequence

On-line material: color figures

1. INTRODUCTION

Prior to the discovery of brown dwarfs (Becklin & Zuckerman 1988; Nakajima et al. 1995; Oppenheimer et al. 1995), the main stellar sequence ended with spectral type M. Stars of spectral type M are characterized by the appearance of deep molecular absorption bands due to the formation of oxides of refractive elements, such as titanium oxide (TiO) and vanadium oxide (VO). Recent years have seen the extension of the spectral sequence to lower temperatures and substellar masses with two new types, L (with temperatures between 2500 and 1500 K) and T (with temperatures less than 1500 K). L dwarfs are characterized by the absence of TiO and VO absorption, the presence of metal hydrides and strong alkali lines in their optical spectra, and strong water vapor absorption bands in the J, H, and K infrared wave bands (e.g., Martin et al. 1999; Kirkpatrick et al. 1999, 2000). T dwarfs are distinguished by the strengthening of water absorption bands and the onset of methane absorption in J, H, and K (e.g., Burgasser et al. 1999; Geballe et al. 2002). Until the discovery of the T dwarf Gl 229B (Nakajima et al. 1995; Oppenheimer et al. 1995), methane absorption had been seen only in the spectra of the Jovian planets and Titan. Spectroscopic surveys, such as the NIRSPEC Brown Dwarf Spectroscopic Survey (BDSS) at the Keck Observatory (McLean et al. 2003) and others (Geballe et al. 2002), have

begun to systematically characterize M, L, and T dwarfs in the infrared and produce canonical, high signal-to-noise ratio (S/N) spectra of each subtype. Figure 1 shows a number of NIRSPEC spectra from the BDSS (McLean et al. 2000). The transitions between M, L, and T dwarfs can be seen. The appearance (and strengthening) of water absorption at 1.5 and 1.75 μm characterizes the L dwarfs, and the addition of methane at 1.66 μm distinguishes the T dwarfs. Theory suggests that L dwarfs are a mixture of hydrogen-burning stars and substellar brown dwarfs. All T dwarfs have substellar masses.

In order to efficiently detect and classify faint brown dwarfs in imaging surveys, we have devised a set of narrowband near-infrared filters at UCLA that select out their unique molecular features, in particular, H_2O and CH_4. Our filters completely span the H band, centered at 1.495 μm (H_2O), 1.595 μm (continuum), 1.66 μm (CH_4), and 1.75 μm (H_2O). All four bands are approximately 6% wide. The use of the narrow continuum filter provides strong contrast between the H_2O and CH_4 absorption bands. The first application of this technique was reported by Mainzer & McLean (2003) using only two filters and the standard H band.

One of the most difficult aspects of detecting low-mass objects, particularly in young star-forming regions where extinction is high because of the presence of primordial gas and dust, is distinguishing genuine cluster members from foreground or reddened background objects. Using a second H_2O filter at 1.75 μm, we can distinguish between bona fide water absorption and reddening by constructing three-dimensional color-color-color cubes. Reddening now appears as a vector in three dimensions. The cube can now be rotated until the reddening vector is seen face-on, making it disappear. In § 2 we describe the development of photometric indexes using the new filters. Observational verification of the technique is

[1] Department of Physics and Astronomy, University of California, Los Angeles, CA 90095; mclean@astro.ucla.edu.

[2] Jet Propulsion Laboratory, 4800 Oak Grove Drive, Pasadena, CA 91109; amainzer@jpl.nasa.gov.

[3] Canadian Institute for Theoretical Astrophysics, 60 St. George Street, Toronto, ON M5S 3H8, Canada; sievers@cita.utoronto.ca.

[4] Steward Observatory, 933 North Cherry Avenue, Tucson, AZ 85721; eyoung@as.arizona.edu.
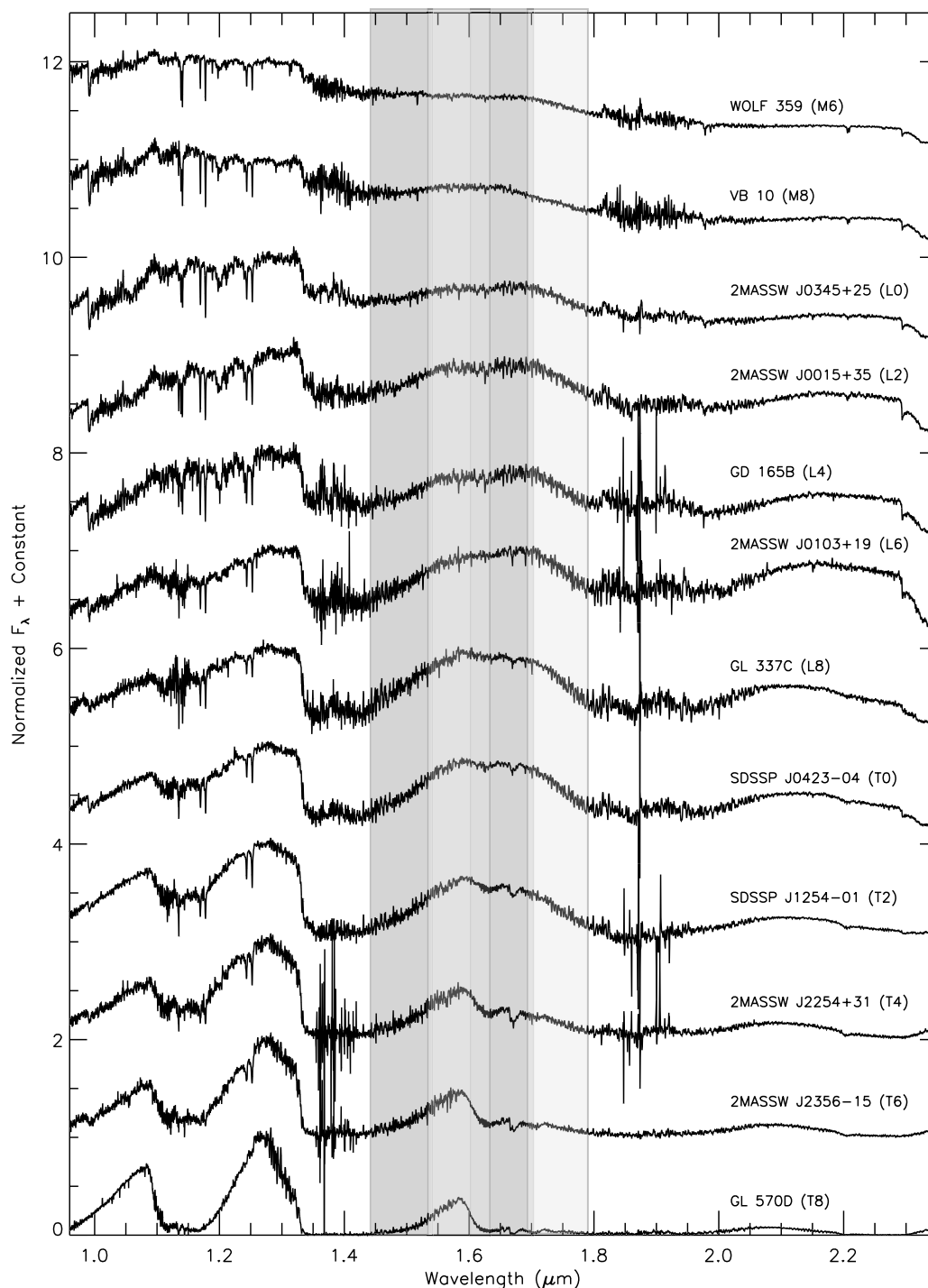
given in § 3, and applications are discussed in § 4. Our conclusions are given in § 5.

2. DEVELOPMENT OF THE PHOTOMETRIC INDEXES

To determine the best set of narrowband indexes to use for spectral classification, a model was created based on the flux-calibrated spectra of 85 objects for which $R \sim 2000$ spectra had already been obtained. These objects ranged in spectral type from B0 main-sequence stars to M9.5 dwarfs, early and late L and T dwarfs, M and K giants and supergiants, and

galaxies. The main-sequence stars were drawn from a database created by Pickles (1998), the M dwarfs from Leggett et al. (2002), the galaxy spectra from M. Rieke (2001, private communication), and the late M, L, and T dwarf spectra from the BDSS.

Using the desired set of trial filter bandpasses as input, the model calculates the magnitudes of each object in each band by numerically integrating the total flux in that band. In addition, the model creates color-magnitude and color-color plots for each set of filter combinations. The primary characteristics

of the T dwarfs are strong H_2O and CH_4 absorption bands in the near-infrared (see Fig. 1). Therefore, a set of indexes based on the strengths of water and methane absorption relative to a continuum band should yield the best discriminator of these objects.

Although strong H_2O and CH_4 features are also found in the K band, it was determined that the best choice was the H band, using features centered at 1.495, 1.66, and 1.75 μm. The locations of the two H_2O filters at 1.495 and 1.75 μm were compromises between maximizing the stellar signature and avoiding the deepest part of the telluric absorption. For ground-based observations, the K band is less sensitive because of thermal background emission from the telescope. Although the J band could be used for the continuum filter, the lower thermal background at the J band is offset by the high extinction from the dust shrouding the stars in young clusters. Both the J and H bands suffer from variable OH emission in the Earth's atmosphere, but the H band provides the best overall sensitivity.

By examining the spectra of L and T dwarfs from the BDSS (McLean et al. 2003), it became obvious that the optimal filters for detecting water and methane should have widths of 0.1 μm, a 6% width for all four filters. The goal was to widen the bandpass as much as possible to allow maximum throughput in that absorption feature, while maintaining sensitivity to the spectral structure. Figure 1 shows the BDSS spectra of several M, L, and T dwarfs with the narrowband filters overlaid. A third narrowband filter centered on 1.595 μm samples the continuum between the water and methane features and provides the best contrast between methane-bearing T dwarfs and everything else. In our previous survey of IC 348 (Mainzer & McLean 2003), we did not have the narrow continuum filter. Instead, we used a broadband H filter as a proxy. This substitution resulted in reduced contrast between various spectral types. A fourth filter centered at 1.75 μm measures the edge of the 1.8 μm water band. Figure 2 shows the as-built filter transmission curves; Table 1 gives the tabulated values for each of the four filters. These curves do not include the effects of either detector response or atmospheric variations; for such a small span in wavelength across the H band, these are basically constant for InSb detectors. The filters were designed to be narrow enough to avoid the atmospheric water bands below 1.4 and above 1.8 μm. Furthermore, since this is a differential photometric classification system, variations across the passbands affect all targets equally and are self-calibrated out.

3. OBSERVATIONS

In order to validate our spectral classification model, we observed seven L and T dwarf standards, as well as a G star (Gizis et al. 2000; Kirkpatrick et al. 2000; Reid et al. 2000; Tinney, Burgasser, & Kirkpatrick 2003; Burgasser et al. 2002; Geballe et al. 2002; Persson et al. 1998). All are field objects whose spectral types are well determined. The goal of these measurements was to determine how well the narrowband photometry agrees with the model. The observations were made using the UCLA narrowband filters installed in FLITECAM, the First Light Camera for SOFIA (Mainzer et al. 2003), at the 3 m Shane Telescope at Mount Hamilton on 2003 May 19–26. FLITECAM (I. McLean, principal investigator) is a 1–5 μm camera with an 8' field of view being developed at UCLA. Conditions were excellent for most of the run, with five out of seven nights photometric. Seeing was typically 0".9–1". Typical integration times for all sources were 27 minutes in each band, resulting in a 3 σ sensitivity of 19.2 mag.

The targets, their H-band magnitudes, and their FLITECAM-measured narrowband magnitudes are listed in Table 2. We can now directly compare the photometric data for these sources with the passband synthesis model. Since we have four bands, we can construct a color-color-color cube. Figure 3 depicts the results of the model, with stars ranging from O to T8, for both unreddened and reddened with an $A_V = 40$ reddening law applied (Rieke & Lebofsky 1985). Figure 4 shows the actual photometric data. Since these are all nearby field objects, they are assumed to have zero reddening. The dashed line in both cubes represents the reddening vector for $A_V = 40$. The cubes
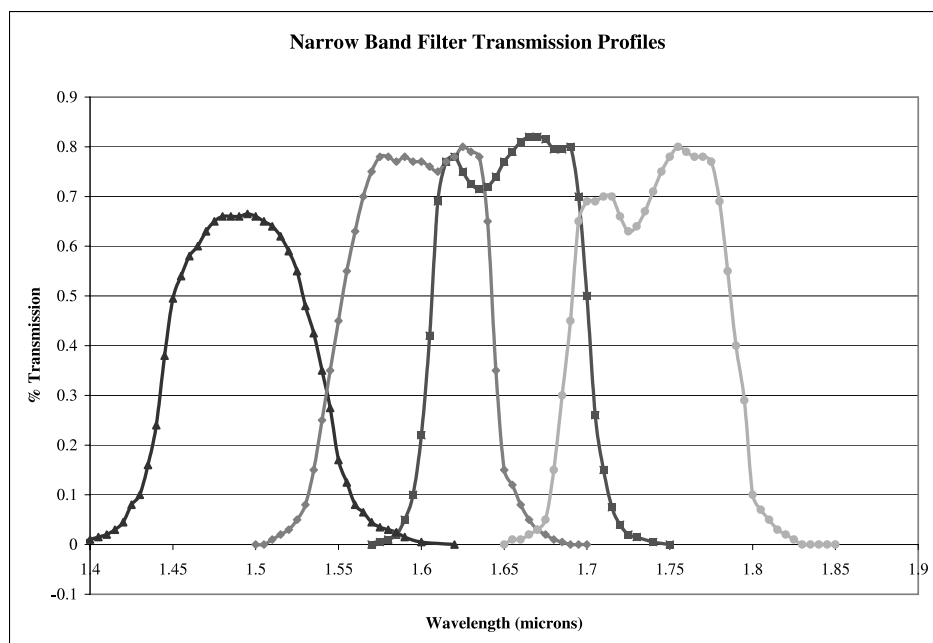

Fig. 2.—Transmission curves of the four custom UCLA narrowband filters. [*See the electronic edition of the Journal for a color version of this figure.*]

TABLE 1
THE TABULATED THROUGHPUT VALUES FOR THE FOUR UCLA NARROWBAND FILTERS

λ (μm)	[1.66 μm] Transmission	λ (μm)	[1.495 μm] Transmission	λ (μm)	[1.595 μm] Transmission	λ (μm)	[1.75 μm] Transmission
1.550	0.00	1.390	0	1.505	0	1.650	0
1.570	0.00	1.395	0	1.510	0.01	1.655	0.01
1.575	0.01	1.400	0.01	1.515	0.02	1.660	0.01
1.580	0.01	1.405	0.02	1.520	0.03	1.665	0.02
1.585	0.02	1.410	0.02	1.525	0.05	1.670	0.03
1.590	0.05	1.415	0.03	1.530	0.08	1.675	0.05
1.595	0.10	1.420	0.05	1.535	0.15	1.680	0.15
1.600	0.22	1.425	0.08	1.540	0.25	1.685	0.30
1.605	0.42	1.430	0.10	1.545	0.35	1.690	0.45
1.610	0.69	1.435	0.16	1.550	0.45	1.695	0.65
1.615	0.77	1.440	0.24	1.555	0.55	1.700	0.69
1.620	0.78	1.445	0.38	1.560	0.63	1.705	0.69
1.625	0.75	1.450	0.50	1.565	0.70	1.710	0.70
1.630	0.73	1.455	0.54	1.570	0.75	1.715	0.70
1.635	0.72	1.460	0.58	1.575	0.78	1.720	0.66
1.640	0.72	1.465	0.60	1.580	0.78	1.725	0.63
1.645	0.74	1.470	0.63	1.585	0.77	1.730	0.64
1.650	0.77	1.475	0.65	1.590	0.78	1.735	0.67
1.655	0.79	1.480	0.66	1.595	0.77	1.740	0.71
1.660	0.81	1.485	0.66	1.600	0.77	1.745	0.75
1.665	0.82	1.490	0.66	1.605	0.76	1.750	0.78
1.670	0.82	1.495	0.67	1.610	0.75	1.755	0.80
1.675	0.82	1.500	0.66	1.615	0.77	1.760	0.79
1.680	0.80	1.505	0.65	1.620	0.78	1.765	0.78
1.685	0.80	1.510	0.64	1.625	0.80	1.770	0.78
1.690	0.80	1.515	0.62	1.630	0.79	1.775	0.77
1.695	0.70	1.520	0.59	1.635	0.78	1.780	0.69
1.700	0.50	1.525	0.55	1.640	0.65	1.785	0.55
1.705	0.26	1.530	0.48	1.645	0.35	1.790	0.40
1.710	0.15	1.535	0.43	1.650	0.15	1.795	0.29
1.715	0.08	1.540	0.35	1.660	0.12	1.800	0.10
1.720	0.04	1.545	0.28	1.665	0.08	1.805	0.07
1.725	0.02	1.550	0.17	1.670	0.03	1.810	0.05
1.730	0.02	1.555	0.13	1.675	0.02	1.815	0.03
1.735	0.01	1.560	0.08	1.680	0.01	1.820	0.02
1.740	0.00	1.565	0.07	1.685	0	1.825	0.01
1.745	0.00	1.570	0.05	1.690	0	1.830	0

can then be rotated so that we are looking down the reddening vector, making it disappear (Figs. 5 and 6). In this way, we can solve for the reddening for each individual object. This technique can be useful in young star-forming regions, where extinction can cause confusion between a reddened background main-sequence star and a water- or methane-bearing young cluster member. The advantage of this technique is that one is not required to make any assumptions or models of average reddening, and it definitively identifies and classifies individual candidates. Using a photometric classification technique can result in great savings in observing time when compared to spectroscopy; indeed, for the faintest targets, accurate spectroscopy may not be possible.

The four physical magnitudes can be transformed into a set of two reddening-free indexes μ_1 and μ_2, from which we can also derive the visual extinction A_V. This is equivalent to finding the two-dimensional projection of the three-dimensional color-color-color cube once it has been rotated to remove the reddening. It is important to note that these reddening-free indexes are derived using the Rieke-Lebofsky reddening law interpolated over the narrowband filter bandpasses. These indexes were calculated by using a least-squares fit to the vector defined by

examining the difference between reddened and unreddened bandpass model colors for spectral types B–L. The equations to transform between the four colors and the new indexes are

$$\mu_1 = 0.92(H_B - H_A) - 0.18(H_B - H_C)$$
$$+ 0.35(H_B - H_D),$$

$$\mu_2 = 0.26(H_B - H_A) + 0.94(H_B - H_C)$$
$$- 0.20(H_B - H_D),$$

$$A_V = 2.95(H_B - H_A) + 5.13(H_B - H_C)$$
$$+ 27.51(H_B - H_D) - 3.37,$$

where H_A is the magnitude at 1.495 μm, H_B at 1.595 μm, H_C at 1.66 μm, and H_D at 1.75 μm.

The reddening-free indexes μ_1 and μ_2 were defined such that the main sequence lies along the μ_1-axis. The agreement between the data and the model can be most easily seen by comparing the reddening-free indexes of the model and the actual data. Figures 7 and 8 show the comparison between the data and model for the μ_1 and μ_2 reddening-free color indexes.

TABLE 2
The G, L, and T Standards Observed with the Custom Narrowband Filters

		MAGNITUDE				
TARGET	SPECTRAL TYPE	H-Band	[1.495 μm]	[1.595 μm]	[1.66 μm]	[1.75 μm]
2MASS 1217111 −031113	T7.5	15.79	16.04	14.98	16.46	16.42
2MASS 13004255 +1912354..........	L1	12.07	12.50	12.14	11.91	11.98
2MASS 1507476 −1627386...........	L5	11.90	12.31	11.76	11.61	11.62
2MASS 15232263 +3014562..........	L8	15.00	15.52	14.86	14.70	14.60
2MASS 1553022 +153236..............	T7	15.92	16.18	15.17	16.34	16.96
SDSS 1750+1759	T3.5	15.97	16.35	15.61	15.83	16.05
2MASS 2254189 +312349..............	T5	14.83	15.21	14.38	14.65	14.88
SJ 9150	G	11.31	11.25	11.26	11.22	11.12

NOTES.—Zero points for [1.595 μm] were determined by comparing objects in the same field of view with known H-band magnitudes (and spectral types determined by using 2MASS colors) to the [1.595 μm] measurements. Zero points for the remaining colors were determined by setting an A star equal to zero color, determining the spectral type of background objects in each field using their 2MASS colors, and setting their narrowband colors appropriately. The [1.595 μm] magnitudes for all objects are accurate to ± 0.03 mag; [1.495 μm], [1.66 μm], and [1.75 μm] magnitudes are accurate to ± 0.07 mag.

It can be seen from these figures that these indexes are most sensitive to L and T dwarfs, with the latest type T dwarfs exhibiting an $\sim$2 mag depletion in the [1.595 μm]−[1.75 μm] colors. The uncertainty in the derived reddening, A_V, is ± 2.5 mag (1 σ) for a photometric accuracy of ± 0.05 mag in all four bands. Note that the extinction determination only applies precisely to main-sequence stars through L dwarfs. The index still yields an estimate of the extinction for T dwarfs, but with diminished accuracy due to the steep structure of T dwarf absorption features, which can shift the

apparent band centers. The amount of inaccuracy expected for the T dwarf sequence reddening is approximately 0.2–0.3 mag, resulting in an extinction uncertainty of 6–8 mag.

Table 3 gives the typical color-color-color indexes for various spectral types, ranging from main-sequence objects through T8 as calculated from the bandpass model. Table 4 gives the color-color-color indexes derived from the as-measured narrowband photometry. These are the tabulated values of Figures 3 and 4. Table 5 gives the reddening-free indexes for the various spectral types as predicted by the bandpass
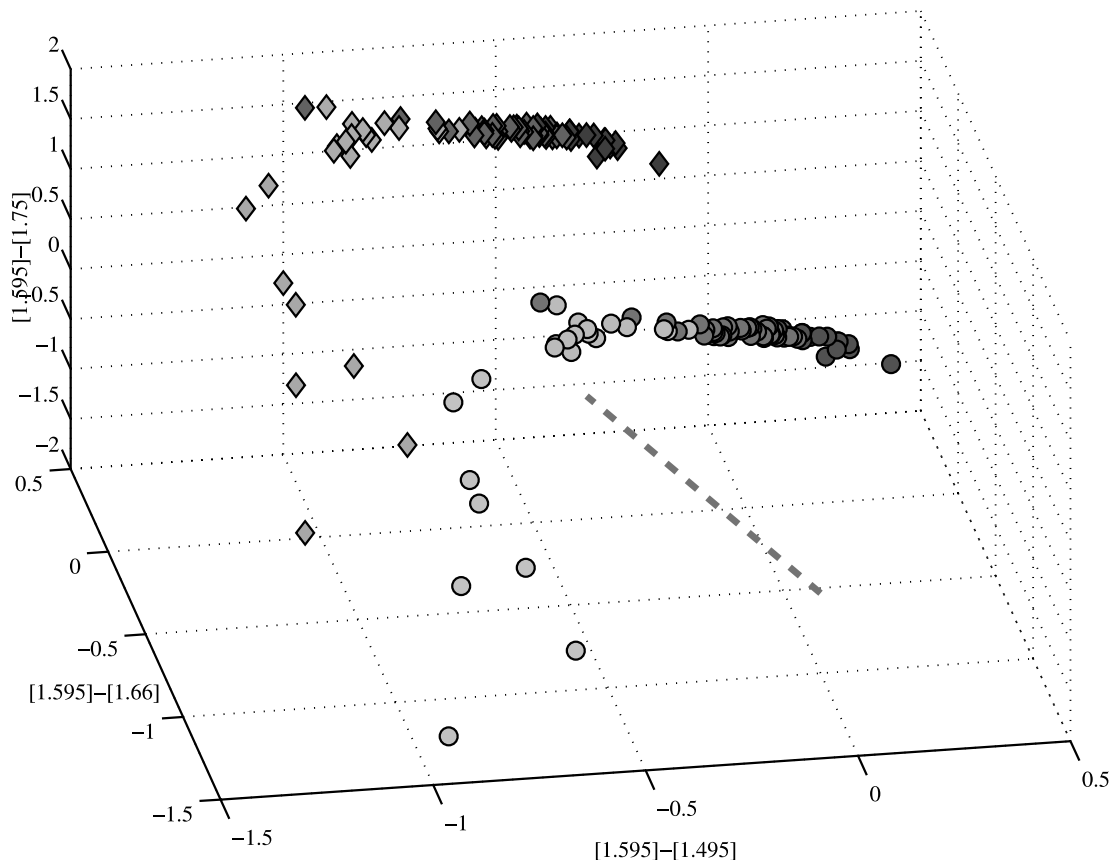

FIG. 3.—Model color-color-color cube, derived by integrating actual spectra over the as-measured filter bandpasses, shown with sources both reddened (*diamonds*) and unreddened (*circles*). The dashed line represents a reddening of $A_V = 40$. [*See the electronic edition of the Journal for a color version of this figure*].
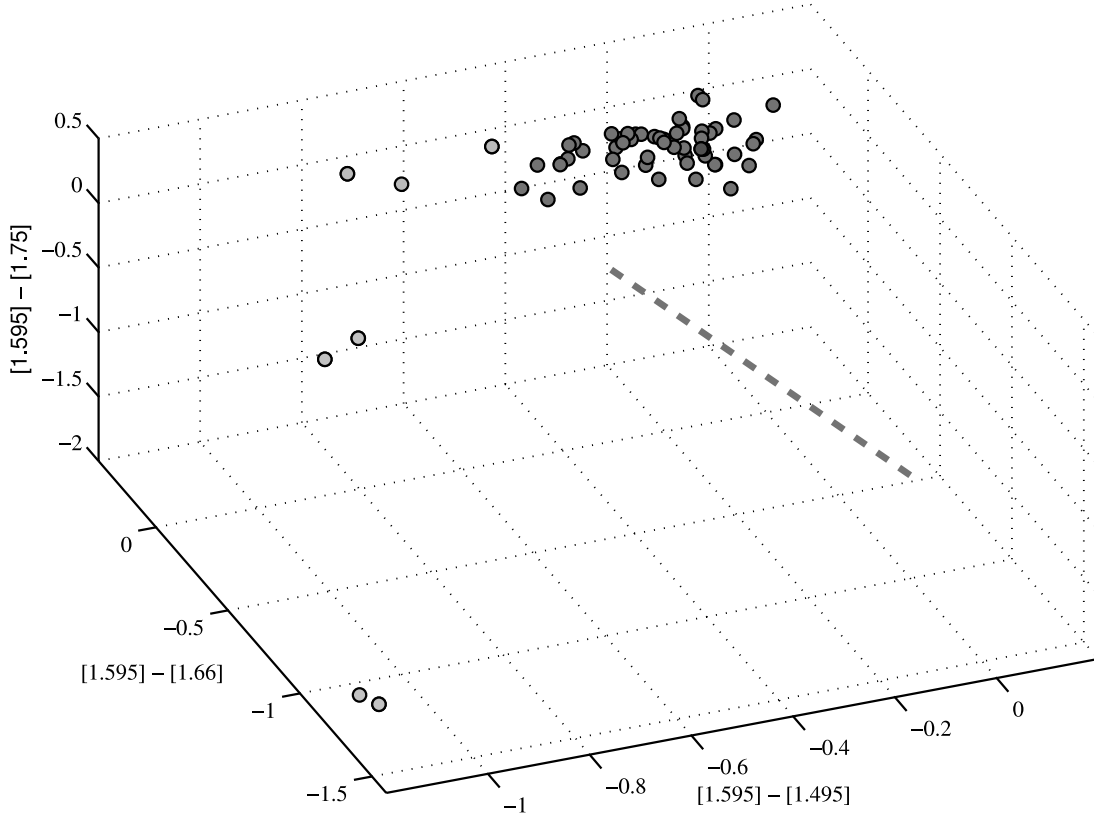
Fig. 4.—Color-color-color cube for the as-measured photometric data. The dashed line represents a reddening of $A_V = 40$. [*See the electronic edition of the Journal for a color version of this figure*].
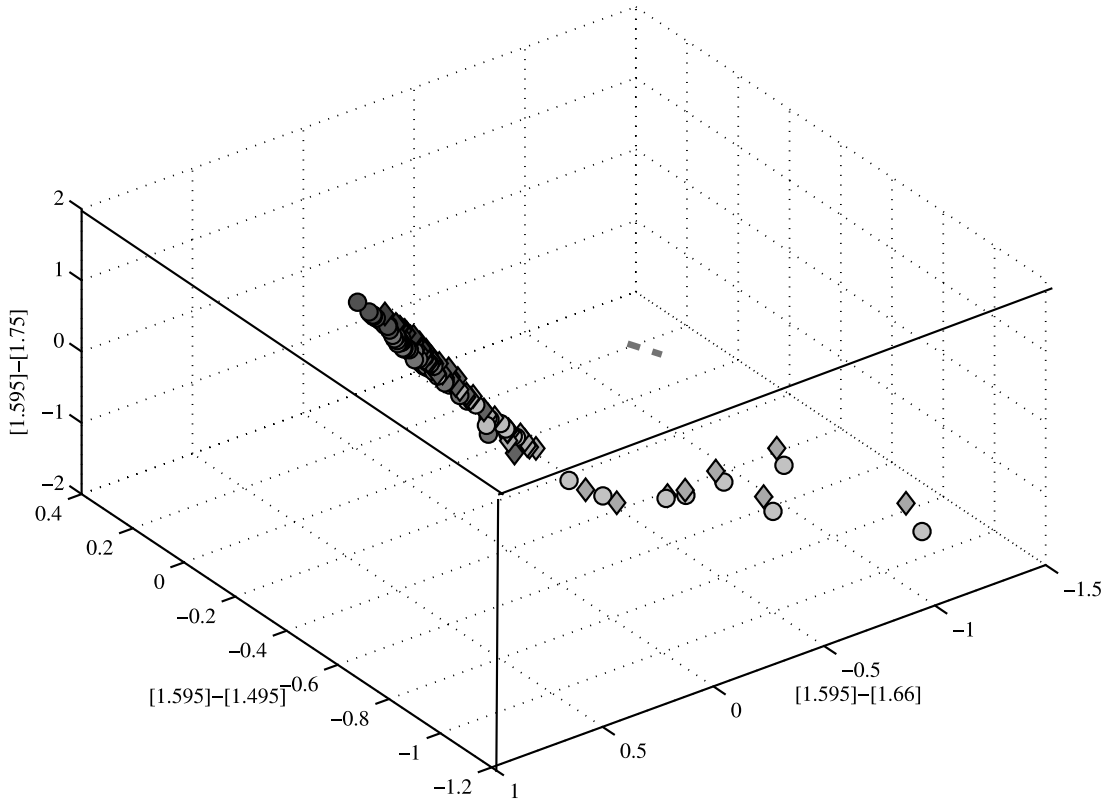

Fig. 5.—Model color-color-color cube, rotated to make the reddening vector disappear. The projection of the stellar sequence along this direction results in two reddening-free indexes, μ_1 and μ_2. [*See the electronic edition of the Journal for a color version of this figure*.]
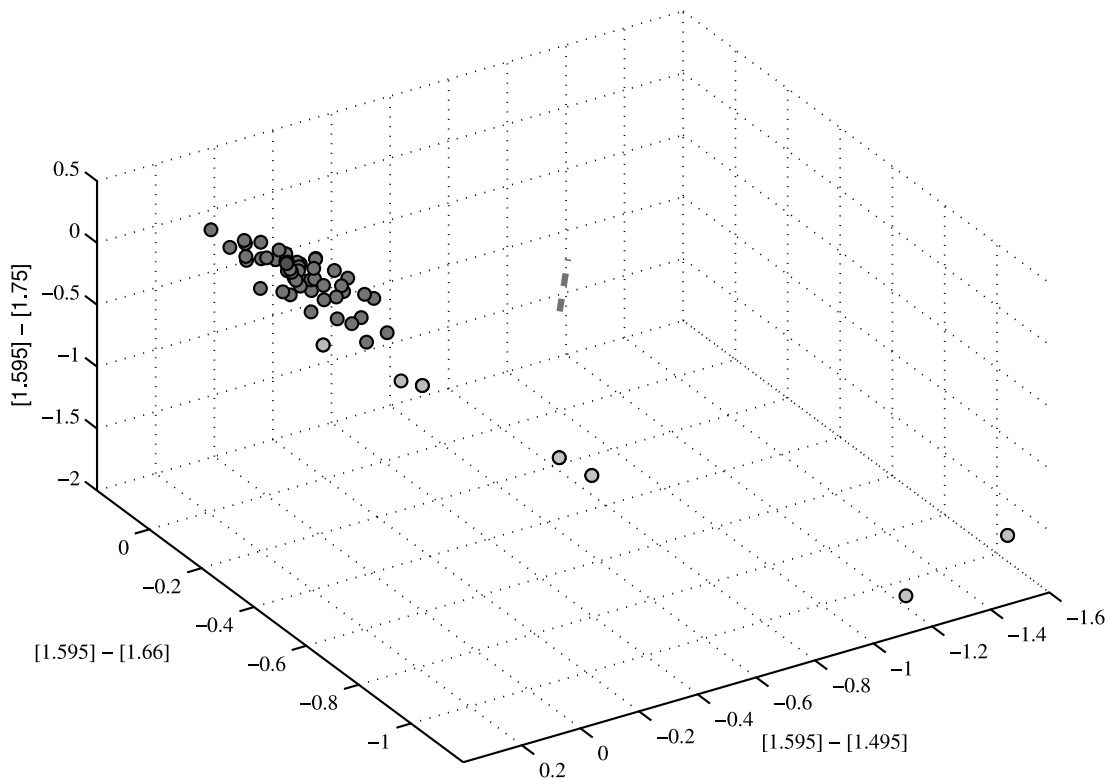
FIG. 6.—Color-color-color cube for the as-measured photometric data, rotated to make the reddening vector disappear. The projection of the stellar sequence along this direction results in two reddening-free indexes, μ_1 and μ_2. [*See the electronic edition of the Journal for a color version of this figure.*]
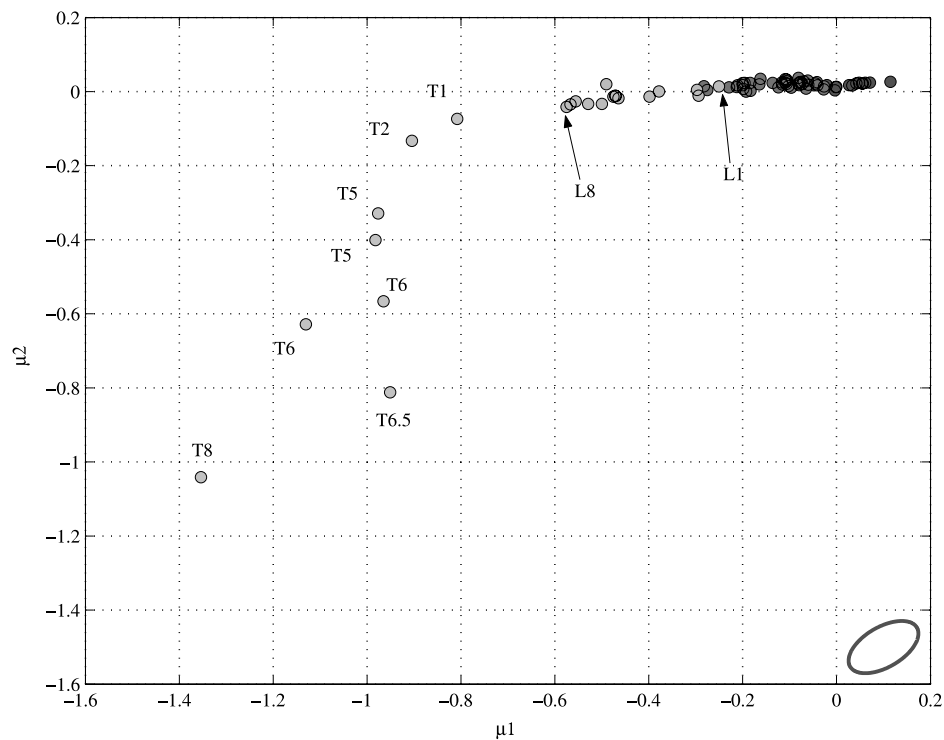

FIG. 7.—Model with colors converted to the reddening-free indexes μ_1 and μ_2. The error ellipse for ±0.05 mag photometry in all four bands is shown at the bottom right of the plot; note that it resembles a line, since most of the error occurs in the direction of the semimajor axis. [*See the electronic edition of the Journal for a color version of this figure.*]
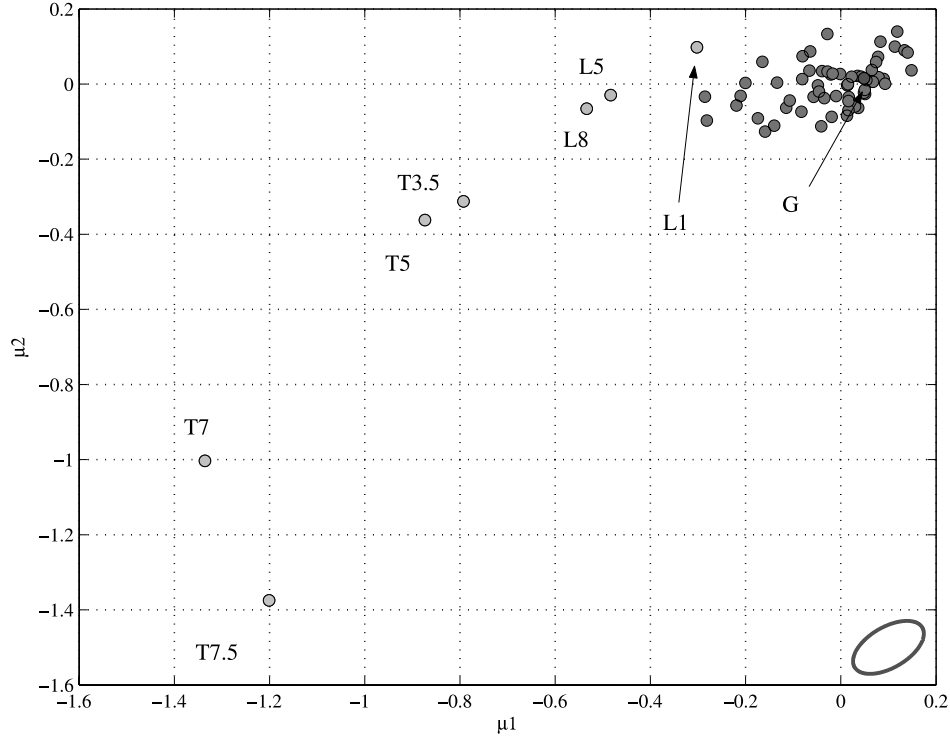
FIG. 8.—As-measured data, with colors converted to the reddening-free indexes μ_1 and μ_2. The error ellipse for ±0.05 mag photometry in all four bands is shown at the bottom right of the plot; note that it resembles a line, since most of the error occurs in the direction of the semimajor axis. [*See the electronic edition of the Journal for a color version of this figure.*]

model. Table 6 gives the reddening-free indexes for the various spectral types derived from the as-measured narrowband photometry. These are the tabulated values of Figures 7 and 8.

The advantage of using FLITECAM to observe brown dwarf standards is that its wide field of view captures many other objects along with the target. This allows us to perform relative photometry between the target and other background stars. For background stars that have known Two Micron All Sky Survey (2MASS) colors, it is possible to estimate their spectral types (Bessell & Brett 1988). Thus, we can use these background stars to calibrate the color-color-color cubes for

each field. This was done by making standard $(J-H)$ versus $(H-K)$ color-color plots from 2MASS data for the background stars, then choosing those objects that appeared to be the least reddened on this color-color plot to serve as calibrators. In each field, there were typically only between one and three such stars available. Thus, the zero-point errors were those associated with few stars. These unreddened background stars were assigned a spectral type based on their JHK colors using Tables 2 and 3 of Bessell & Brett (1988). The [1.595 μm] zero point for a given field was set by equating the [1.595 μm] magnitudes of the calibrator stars with their 2MASS H-band

TABLE 3
OBJECT COLOR INDEXES AS PREDICTED BY THE INTEGRATED BANDPASS MODEL

Spectral Type	[1.595 μm]−[1.495 μm]	[1.595 μm]−[1.66 μm]	[1.595 μm]−[1.75 μm]
B0–A5	0.00 to 0.15	−0.03 to 0.05	−0.07 to 0.12
F0–G8	0.00 to 0.06	0.02 to 0.05	0.03 to 0.013
K–M3	−0.11 to −0.05	0.05 to 0.09	0.09 to 0.17
M4–M5	−0.15 to −0.09	0.08 to 0.11	0.09 to 0.17
M6–M7	−0.27 to −0.13	0.07 to 0.13	0.09 to 0.17
M8–M8.5	−0.27 to −0.23	0.09 to 0.11	0.11 to 0.13
M9–M9.5	−0.35 to −0.25	0.10 to 0.15	0.14 to 0.19
L0–L1	−0.35 to −0.30	0.12 to 0.13	0.14 to 0.15
L2	−0.36 to −0.59	0.13 to 0.25	0.16 to 0.28
L3–L4	−0.54 to −0.48	0.15 to 0.16	0.09 to 0.21
L5–L7	−0.61 to −0.53	0.13 to 0.18	0.00 to 0.20
L7.5–L8	−0.62 to −0.57	0.14 to 0.15	0.05 to 0.14
T1–T2	−0.87 to −0.79	0.04 to 0.11	−0.27 to −0.17
T5	−0.88 to −0.87	−0.33 to −0.23	−0.67 to −0.59
T6	−0.97 to −0.81	−0.61 to −0.57	−1.00 to −0.92
T6.5	−0.75	−0.91	−1.21
T8	−1.09	−1.14	−1.59

TABLE 4
THE AS-MEASURED COLOR INDEXES OF THE OBJECTS

Spectral Type	[1.595 μm]−[1.495 μm]	[1.595 μm]−[1.66 μm]	[1.595 μm]−[1.75 μm]
G............................	0.01	0.04	0.13
L1	−0.36	0.23	0.16
L5	−0.55	0.15	0.14
L8	−0.66	0.16	0.26
T3.5	−0.73	−0.22	−0.44
T5	−0.83	−0.27	−0.50
T7	−1.01	−1.17	−1.79
T7.5	−1.06	−1.48	−1.44

magnitudes. Since the calibrator stars were chosen to be F–K stars, the H-band magnitude is a reasonable representation of the continuum feature at 1.595 μm. Zero points of the remaining three colors were set by adjusting the calibrator stars' narrowband magnitudes to match their 2MASS-derived spectral types, such that an A star is defined to have zero color ($H_A = H_B = H_C = H_D = 0$). By assigning these background objects with known spectral types to their appropriate color values, we can calibrate the photometry of the brown dwarfs. This makes it possible to combine fields measured on different nights in variable weather conditions into a single color-color-color cube. Comparison between 2MASS broadband H and [1.595 μm] magnitudes showed agreement to within ±0.04 mag for the calibrator stars. This error is derived as follows: The 2MASS magnitudes are accurate to ∼±0.03 mag; this is added in quadrature with the FLITECAM photometry of individual objects within a single field, which is accurate to ±0.03 mag. The errors for the [1.495 μm], [1.66 μm], and [1.75 μm] bands were measured to be ±0.07 mag. Although photometry was measured to within ±0.03 mag in all of these bands, the uncertainty in the assignment of zero points using the 2MASS colors of background objects is the dominant error source. This was derived by calculating the distribution in the μ_2-axis when plotting all the background objects for each field in μ_1-μ_2 space. For A through early M stars, the variation in the μ_2-axis should have been ±0.01 mag according to the bandpass model (see Table 5). Therefore, any variations greater than this are

attributable to a combination of photometric error and zero-point error. It is important to note that the zero-point errors of the other three bands are reduced greatly by performing relative photometry between objects in the same field of view, e.g., in a single pointing in a young cluster.

The advantage of this system is that it becomes more sensitive and better able to determine spectral type as object temperature decreases; thus, it is most sensitive to the coolest objects. Based on these results, we now have a system that can classify A through early M stars to within ±2 spectral types, late-type M and L dwarfs to within ±0.3 spectral types, and T dwarfs to within ±0.1 types (1 σ) for objects measured with S/N = 20 (±0.05 mag photometry). Thus, a G star's spectral type would appear to be between A and early M; an M9 dwarf would appear to be between M6 and L3; and a T6 would appear to be between T5 and T7. Since μ_1 and μ_2 both use all four fluxes, their errors are correlated and form an error ellipse. This ellipse is plotted in the corner of Figure 7 for the case of all bands having ±0.05 mag errors. The directions of the axes of the ellipse are given by the eigenvectors of the covariance matrix of μ_1 and μ_2 (assuming independent, equal photometric errors in all four bands). The magnitudes of the semimajor and semiminor error ellipse axes are given by the square roots of the eigenvalues of the covariance matrix multiplied by the per band photometric errors. For ±0.05 mag errors in all four bands, the projection of the error ellipse along the B–L dwarf sequence is 0.07 mag. Since the difference between early and late L dwarfs spans 0.3 mag (see Table 5), we can determine spectral type to within $\frac{1}{4}$ of a spectral type, or ∼±0.3 spectral types (1 σ). For T dwarfs, the error ellipse's semimajor axis lies roughly along the same direction as the T dwarf sequence in Figure 7. Thus, ±0.05 mag errors in all four bands yields an error of ±0.08 mag in the semimajor axis direction. Since the T dwarf sequence spans a length of ∼1.2 mag in Figure 7, we can discern a difference of approximately ±0.1 spectral types (1 σ).

TABLE 5
THE REDDENING-FREE INDEXES PREDICTED FOR VARIOUS SPECTRAL
TYPES COMPUTED FROM THE INTEGRATED BANDPASS MODEL

Spectral Type	μ_1	μ_2
B0–A5	0.00 to 0.11	0.00 to 0.03
F0–G8	0.03 to 0.06	0.00 to 0.03
K–M3	−0.07 to 0.00	0.00 to 0.03
M4–M5	−0.11 to −0.07	0.00 to 0.03
M6–M7	−0.21 to −0.08	0.00 to 0.04
M8–M8.5	−0.23 to −0.18	0.00 to 0.02
M9–M9.5	−0.28 to −0.19	0.00 to 0.02
L0–L1	−0.30 to −0.25	0.00 to 0.02
L2	−0.49 to −0.29	0.00 to 0.02
L3–L4	−0.47 to −0.40	−0.02 to 0.00
L5–L7	−0.57 to −0.47	−0.03 to −0.01
L7.5–L8	−0.58 to −0.50	−0.04 to −0.03
T1–T2	−0.90 to −0.81	−0.13 to −0.7
T5	−0.98 to −0.97	−0.40 to −0.33
T6	−1.13 to −0.96	−0.63 to −0.57
T6.5	−0.95	−0.81
T8	−1.35	−1.04

TABLE 6
THE AS-MEASURED REDDENING-FREE INDEXES FOR THE OBJECTS

Spectral Type	μ_1	μ_2
G..	0.05	0.01
L1	−0.32	0.09
L5	−0.48	−0.03
L8	−0.55	−0.07
T3.5	−0.79	−0.31
T5	−0.89	−0.37
T7	−1.35	−1.00
T7.5	−1.21	−1.38

4. FUTURE APPLICATIONS

The advantage of this technique is that it can be used to obtain spectral classifications and reddenings for individual objects detected in large-area surveys. This technique is particularly well suited to surveys of young clusters, where the objects' youth and correspondingly increased brightness make it possible to detect much lower mass objects at farther distances and where extinction is a significant factor. It is possible that changes in the objects' spectra due to decreased gravity may alter their spectral features (e.g., Lucas & Roche 2000), producing changes in the observed narrowband colors. However, in our previous survey of IC 348 (Mainzer & McLean 2003), although we found an average ∼0.2 mag difference between field objects and young M dwarfs, their relative narrowband colors still served as an effective means of obtaining their spectral types. Future identifications of young low-mass objects will determine how gravity and age influence narrowband colors. Narrowband photometry can also be used as an effective means to find field brown dwarfs, as well as serve as a useful follow-up method for objects found via 2MASS or SIRTF.

5. CONCLUSIONS

We have designed a new set of four near-infrared narrowband filters spanning the H band that can be used to simultaneously identify and classify stars and brown dwarfs. By breaking the H band into four bands centered on characteristic molecular features of cool stars and brown dwarfs, we are essentially performing extremely low resolution spectroscopy. The advantage of narrowband photometry is that an estimate of reddening-free spectral type is provided for all objects in the field of view, avoiding the costly process of obtaining spectra for each individual object. By using four filters, we now have a means to break the degeneracy between increased water absorption and reddening. We have constructed a model using actual spectra and the as-measured narrowband filter transmission curves. By observing a number of objects whose spectral types were previously known with narrowband filters, we have confirmed the accuracy of the system. We have devised a methodology for obtaining the spectral types of various background stars in the same field of view as the targets from 2MASS, thus allowing us to combine observations made on different nights under variable weather conditions. For objects measured with $S/N = 20$ (±0.05 mag photometry), we can classify A through early M stars to within ±2 spectral types, late-type M and L dwarfs to within ±0.3 spectral types, and T dwarfs to within ±0.1 types (1 σ). The two new reddening-free indexes and the extinction we have derived from the narrowband colors, μ_1, μ_2, and A_V, make this system particularly suitable for use in young clusters, where extinction is high. The use of narrowband photometry can provide an efficient means of obtaining spectral types of a great number of objects simultaneously, both in young clusters and in the field.

REFERENCES

Becklin, E. E., & Zuckerman, B. 1988, Nature, 336, 656
Bessell, M. S., & Brett, J. M. 1988, PASP, 100, 1134
Burgasser, A. J., et al. 1999, ApJ, 522, L65
———. 2002, ApJ, 564, 421
Geballe, T. R., et al. 2002, ApJ, 564, 466
Gizis, J. E., Monet, D. G., Reid, I. N., Kirkpatrick, J. D., Liebert, J., & Williams, R. J. 2000, AJ, 120, 1085
Kirkpatrick, J. D., Reid, I. N., Liebert, J., Gizis, J. E., Burgasser, A. J., Dahn, C. C., Nelson, B., & Williams, R. J. 2000, AJ, 120, 447
Kirkpatrick, J. D., et al. 1999, ApJ, 519, 802
Leggett, S. K., et al. 2002, ApJ, 564, 452
Lucas, P. W., & Roche, P. F. 2000, MNRAS, 314, 858
Mainzer, A. K., & McLean, I. S. 2003, ApJ, 597, 555
Mainzer, A. K., et al. 2003, Proc. SPIE, 4857, 21
Martin, E. L., Delfosee, X., Basri, G., Goldman, B., Forveille, T., & Zapatero Osorio, M. R. 1999, AJ, 118, 2466

McLean, I. S., McGovern, M. R., Burgasser, A. J., Kirkpatrick, J. D., Prato, L., & Kim, S. S. 2003, ApJ, 596, 561
McLean, I. S., et al. 2000, Proc. SPIE, 4008, 1048
Nakajima, T., Oppenheimer, B. R., Kulkarni, S. R., Golimowski, D. A., Matthews, K., & Durrance, S. T. 1995, Nature, 378, 463
Oppenheimer, B. R., Kulkarni, S. R., Matthews, K., & Nakajima, T. 1995, Science, 270, 1478
Persson, S. E., Murphy, D. C., Krzeminski, W., Roth, M., & Rieke, M. J. 1998, AJ, 116, 2475
Pickles, A. 1998, PASP, 110, 863
Reid, I. N., Kirkpatrick, J. D., Gizis, J. E., Dahn, C. C., Monet, D. G., Williams, R. J., Liebert, J., & Burgasser, A. J. 2000, AJ, 119, 369
Rieke, G. H., & Lebofsky, M. J. 1985, ApJ, 288, 618
Tinney, C. G., Burgasser, A. J., & Kirkpatrick, J. D. 2003, AJ, 126, 975